PROCEEDINGS OF SPIE

SPIEDigitalLibrary.org/conference-proceedings-of-spie

Measuring 3D molecular orientation and rotational mobility using a Tri-spot point spread function

Oumeng Zhang, Tianben Ding, Jin Lu, Hesam Mazidi, Matthew D. Lew

Oumeng Zhang, Tianben Ding, Jin Lu, Hesam Mazidi, Matthew D. Lew, "Measuring 3D molecular orientation and rotational mobility using a Tri-spot point spread function," Proc. SPIE 10500, Single Molecule Spectroscopy and Superresolution Imaging XI, 105000B (20 February 2018); doi: 10.1117/12.2287004

SPIE.

Event: SPIE BiOS, 2018, San Francisco, California, United States

Measuring 3D molecular orientation and rotational mobility using a Tri-spot point spread function

Oumeng Zhang[a], Tianben Ding[a], Jin Lu[a], Hesam Mazidi[a], Matthew D. Lew*[a]
[a]Department of Electrical and Systems Engineering, Washington University in St. Louis, 1 Brookings Drive, St. Louis, MO, USA 63130

ABSTRACT

We present a method to measure the molecular orientation and rotational mobility of single-molecule emitters by designing and implementing a Tri-spot point spread function. It can measure all degrees of freedom related to molecular orientation and rotational mobility. Its design is optimized by maximizing the theoretical limit of its measurement precision. We evaluate the precision and accuracy of the Tri-spot PSF by measuring the orientation and effective rotational mobility of single fluorescent molecules embedded in a polymer matrix.

Keywords: single-molecule imaging, fluorescence microscopy, point spread function engineering, phase mask design

1. INTRODUCTION

Single-molecule imaging techniques have become invaluable for probing the heterogeneity of both biological and abiological systems with nanoscale resolution. The unique versatility of these nanometer-sized probes stems from their ability to encode interactions with their local environment into the fluorescence that they emit, as evidenced by heterogeneous absorption spectra of single molecules first observed decades ago[1]. Recently, these techniques have gained popularity for their capability to produce images of structures within living cells with resolution beyond the Abbé diffraction limit (~250 nm for visible light). Super-resolution optical techiques[2–4] that repeatedly record the position of individual molecules over time to construct super-resolved images are known collectively as single-molecule localization microscopes (SMLM).

Beyond tracking the position and spectra of individual molecules, probing their orientation has provided valuable insight into a number of biological systems[5], including molecular motors[6–9]. Molecular orientation can be inferred by measuring a molecule's fluorescence intensity in response to varying polarizations of excitation light[10], measuring its fluorescence intensity in one or more polarized detection channels[11], measuring the angular spectrum of its fluorescence emission[12,13], or some combination of the aforementioned techniques.

Recently, point spread function (PSF) engineering, or direct design of an optical instrument's impulse response, has been used to great advantage to augment super-resolution microscopes with 3D imaging[14–18] and even multicolor[19] capabilities. Other techniques, such as the bisected[20] and quadrated[21] pupils and the double-helix[22] PSF, have been designed to measure the orientation of individual fluorescent molecules.

Here, we describe an intensity-based image-formation model for our microscope in response to a dipole-like emitter. By examining this model, we design the Tri-spot PSF, which contains the same number of spots as the number of orientational degrees of freedom within the model. The Tri-spot PSF enables the simultaneous measurement of molecular orientation and rotational mobility with high signal-to-background ratio. We evaluate the precision and accuracy of orientation measurements with the Tri-spot PSF via imaging simulations and experimental measurements of fluorescent molecules.

2. TRI-SPOT PSF DESIGN

2.1 Forward imaging model

We model a single fluorescent molecule as an oscillating electric dipole with an orientation parametrized by a unit vector $\boldsymbol{\mu}$ given by

*mdlew@wustl.edu; phone 1-314-935-6790; fax 1-314-935-7500; lewlab.wustl.edu

Single Molecule Spectroscopy and Superresolution Imaging XI, edited by Jörg Enderlein, Ingo Gregor, Zygmunt Karol Gryczynski, Rainer Erdmann, Felix Koberling, Proc. of SPIE Vol. 10500, 105000B
 · doi: 10.1117/12.2287004

$$\boldsymbol{\mu} = \begin{bmatrix} \mu_x \\ \mu_y \\ \mu_z \end{bmatrix} = \begin{bmatrix} \sin\theta\cos\phi \\ \sin\theta\sin\phi \\ \cos\theta \end{bmatrix} \tag{1}$$

where μ_x, μ_y, and μ_z denote the projection of $\boldsymbol{\mu}$ onto each Cartesian axis. We can also use the polar angle θ and azimuthal angle ϕ in spherical coordinates to represent this vector. After modeling the propagation of light through the objective lens and tube lens, the intensity distribution of the electric field in the image plane is given by[13]

$$I_{x(y)} = I_0 \begin{bmatrix} B_{\mathrm{XX},x(y)} \\ B_{\mathrm{YY},x(y)} \\ B_{\mathrm{ZZ},x(y)} \\ B_{\mathrm{XY},x(y)} \\ B_{\mathrm{XZ},x(y)} \\ B_{\mathrm{YZ},x(y)} \end{bmatrix}^T \begin{bmatrix} \mu_x^2 \\ \mu_y^2 \\ \mu_z^2 \\ \mu_x\mu_y \\ \mu_x\mu_z \\ \mu_y\mu_z \end{bmatrix} = I_0 \boldsymbol{B}_{x(y)} \boldsymbol{M} \tag{2}$$

where I_0 gives the total number of photons captured in the image and $\boldsymbol{B}_{x(y)} = \left[B_{\mathrm{XX},x(y)}, \ldots, B_{\mathrm{YZ},x(y)}\right]$ are the basis images of the system in response to a dipole emitter whose orientational second moments are given by $\boldsymbol{M} = \left[\mu_x^2, \ldots, \mu_y\mu_z\right]^T$. The subscripts $x(y)$ refer to x-polarized and y-polarized images, respectively, if a polarizing beamsplitter is used to create two imaging channels[22]. Note that the basis images are independent of emitter orientation. Therefore, we wish to design the basis images $\boldsymbol{B}_{x(y)}$ to maximize the precision of measuring the orientational second-moments $\boldsymbol{M}$ of a dipole-like emitter.

If the emitter is rotating over time, then the orientational second-moment trajectories can be integrated over the camera's exposure time T to model the resulting image:

$$I_{x(y)} = \frac{I_0}{T} \boldsymbol{B}_{x(y)} \begin{bmatrix} \int_0^T \mu_x(t)^2 \, \mathrm{d}t \\ \int_0^T \mu_y(t)^2 \, \mathrm{d}t \\ \int_0^T \mu_z(t)^2 \, \mathrm{d}t \\ \int_0^T \mu_x(t)\mu_y(t) \, \mathrm{d}t \\ \int_0^T \mu_x(t)\mu_z(t) \, \mathrm{d}t \\ \int_0^T \mu_y(t)\mu_z(t) \, \mathrm{d}t \end{bmatrix} = I_0 \boldsymbol{B}_{x(y)} \begin{bmatrix} \langle \mu_x(t)^2 \rangle \\ \langle \mu_y(t)^2 \rangle \\ \langle \mu_z(t)^2 \rangle \\ \langle \mu_x(t)\mu_y(t) \rangle \\ \langle \mu_x(t)\mu_z(t) \rangle \\ \langle \mu_y(t)\mu_z(t) \rangle \end{bmatrix} \tag{3}$$

where $\langle \cdot \rangle$ denotes a temporal average. If a nanoscale emitter is composed of several or many independent dipole-like emitters, then the integrals over time in Eq. (3) can be replaced by discrete sums over the ensemble of emitters. For example, an isotropic emitter has second moments $\boldsymbol{M} = [1/3, 1/3, 1/3, 0, 0, 0]^T$, while a molecule fixed in orientation $\boldsymbol{\mu}$ has second moments $\boldsymbol{M} = \left[\mu_x^2, \mu_y^2, \mu_z^2, \mu_x\mu_y, \mu_x\mu_z, \mu_y\mu_z\right]^T$.

2.2 Designing the Tri-spot PSF

As inspiration, we examine the orientation-sensing strategy of the bisected[20] and quadrated[21] phase masks and note that these phase masks split the standard PSF into 2 or 4 spots, respectively, in order to measure molecular orientation. To maximize signal-to-noise ratio under shot noise-limited conditions, which scales as $\sqrt{N}$, where N is the number of photons detected, we wish to minimize the number of spots within our PSF while maintaining sufficient degrees of freedom to measure all second moments of $\boldsymbol{M}$. Due to the definition of $\boldsymbol{\mu}$ (Eqn. (1)), we note that $\langle \mu_x(t)^2 \rangle + \langle \mu_y(t)^2 \rangle + \langle \mu_z(t)^2 \rangle = 1$. Therefore, we desire a PSF that can measure 5 orientational and 1 brightness degree of freedom – thus, a 6-spot PSF. If we utilize an imaging system with two polarization channels, then a PSF containing 3 spots, or the Tri-spot PSF, will suffice.

Utilizing an existing vectorial diffraction model[13], we tested various phase mask designs that split the back focal plane, or pupil plane, of the microscope into three partitions. We placed a linear phase ramp within each partition to create three off-center, focused spots in the imaging plane. The arrangement of spots was designed to be a triangle to avoid assignment ambiguity resulting from the absence of one spot. The partition shapes within the Tri-spot phase mask were designed to avoid orientation measurement degeneracies like the one shown in Figure 1.

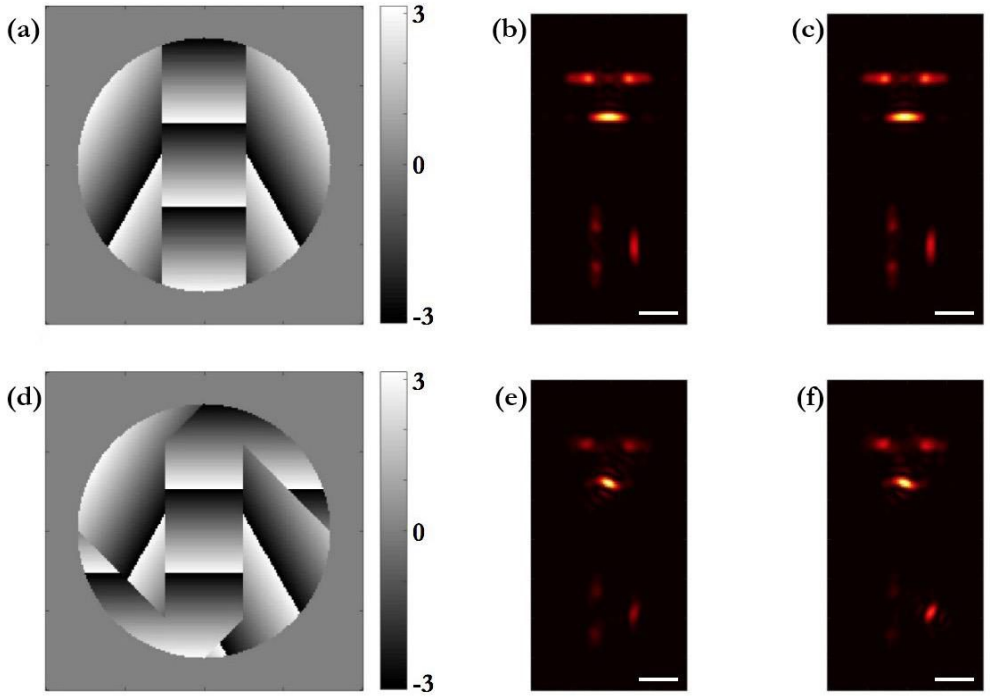

Figure 1. Tri-spot mask and PSF before and after enhancing orientational sensitivity. Before enhancing the $\mu_x\mu_y$ sensitivity of (a) the Tri-spot phase mask (color bar in units of radians), the image of an emitter with (b) molecular orientation $[\mu_x = 0.866, \mu_y = 0.5]$ is very similar to that for (c) orientation $[\mu_x = 0.866, \mu_y = -0.5]$. After reshaping the partitions of (d) the Tri-spot phase mask, (e) the orientation $[\mu_x = 0.866, \mu_y = 0.5]$ is easily distinguishable from (f) orientation $[\mu_x = 0.866, \mu_y = -0.5]$ in the image plane. For all images of the Tri-spot PSF in this work, the top half corresponds to the x-polarized PSF (I_x), and the bottom half corresponds to the y-polarized PSF (I_y). Scale bar: 1 μm.

The basis images $\boldsymbol{B}_{x(y)}$ of the Tri-spot PSF are shown in Figure 2. We model the total number of photons contained within each spot using a vector $\boldsymbol{I}_{\text{spot}} = \left[I_{\text{x1}}, I_{\text{x2}}, I_{\text{x3}}, I_{\text{y1}}, I_{\text{y2}}, I_{\text{y3}}\right]^T$. Therefore, a simplified forward imaging model for the Tri-spot PSF is given by

$$\boldsymbol{I}_{\text{spot}} = I_0 \begin{bmatrix} B_{\text{XX,x1}} & B_{\text{YY,x1}} & B_{\text{ZZ,x1}} & B_{\text{XY,x1}} & B_{\text{XZ,x1}} & B_{\text{YZ,x1}} \\ B_{\text{XX,x2}} & B_{\text{YY,x2}} & B_{\text{ZZ,x2}} & B_{\text{XY,x2}} & B_{\text{XZ,x2}} & B_{\text{YZ,x2}} \\ B_{\text{XX,x3}} & B_{\text{YY,x3}} & B_{\text{ZZ,x3}} & B_{\text{XY,x3}} & B_{\text{XZ,x3}} & B_{\text{YZ,x3}} \\ B_{\text{XX,y1}} & B_{\text{YY,y1}} & B_{\text{ZZ,y1}} & B_{\text{XY,y1}} & B_{\text{XZ,y1}} & B_{\text{YZ,y1}} \\ B_{\text{XX,y2}} & B_{\text{YY,y2}} & B_{\text{ZZ,y2}} & B_{\text{XY,y2}} & B_{\text{XZ,y2}} & B_{\text{YZ,y2}} \\ B_{\text{XX,y3}} & B_{\text{YY,y3}} & B_{\text{ZZ,y3}} & B_{\text{XY,y3}} & B_{\text{XZ,y3}} & B_{\text{YZ,y3}} \end{bmatrix} \boldsymbol{M} = I_0 \boldsymbol{B}_{\text{spot}} \boldsymbol{M} \tag{4}$$

where $\boldsymbol{B}_{\text{spot}}$ is a basis matrix that represents the brightness of each spot of the Tri-spot PSF in response to each component of the orientational second-moment vector $\boldsymbol{M}$. Note that for the Tri-spot PSF, each column of $\boldsymbol{B}_{\text{spot}}$ is linearly independent, which indicates that there is a one-to-one correspondence of the spot brightness vector $\boldsymbol{I}_{\text{spot}}$ with the orientation second moments $\boldsymbol{M}$. Thus, the Tri-spot PSF can measure all degrees of freedom related to the second moment of molecular orientation.

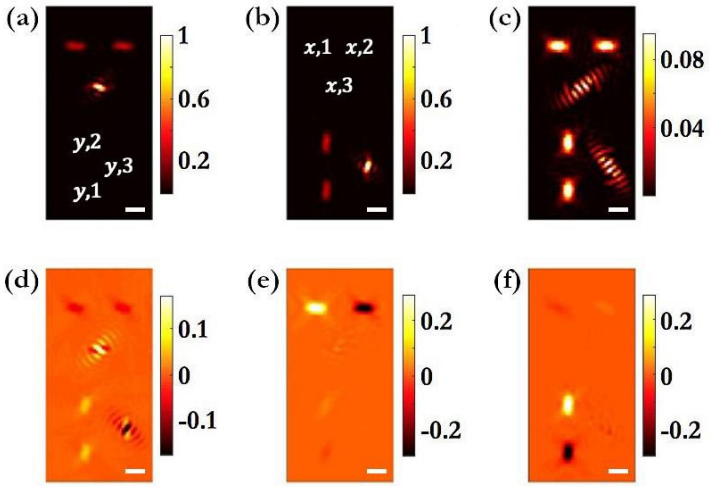

Figure 2. Basis images of the Tri-spot PSF: (a) $B_{\mathrm{XX},x(y)}$, (b) $B_{\mathrm{YY},x(y)}$, (c) $B_{\mathrm{ZZ},x(y)}$, (d) $B_{\mathrm{XY},x(y)}$, (e) $B_{\mathrm{XZ},x(y)}$, and (f) $B_{\mathrm{YZ},x(y)}$. The images are normalized by the total intensity of the brightest basis images, $B_{XX,x}$ and $B_{YY,y}$. Labels $x1, \ldots y3$ assign each spot within each basis image B to the $\boldsymbol{B}_{\mathrm{spot}}$ matrix in the simplified forward imaging model. Scale bar: 1 μm.

3. ORIENTATION PRECISION AND ACCURACY

3.1 Measuring molecular orientation using a maximum likelihood estimator

We tested the performance of the Tri-spot PSF for measuring molecular orientation *in silico* using a maximum likelihood estimator (MLE). Here, we utilize the result that the time-average of any temporal trajectory of molecular orientation $\boldsymbol{\mu}(t) = \left[\mu_x(t), \mu_y(t), \mu_z(t)\right]^T$ can be written as an equivalent second moment vector $\boldsymbol{M}$ given by[10]

$$\langle \mu_x(t)^2 \rangle = \gamma {\mu'_x}^2 + (1-\gamma)/3 \tag{5}$$

$$\langle \mu_y(t)^2 \rangle = \gamma {\mu'_y}^2 + (1-\gamma)/3 \tag{6}$$

$$\langle \mu_z(t)^2 \rangle = \gamma {\mu'_z}^2 + (1-\gamma)/3 \tag{7}$$

$$\langle \mu_x(t)\mu_y(t) \rangle = \gamma \mu'_x \mu'_y \tag{8}$$

$$\langle \mu_x(t)\mu_z(t) \rangle = \gamma \mu'_x \mu'_z \tag{9}$$

$$\langle \mu_y(t)\mu_z(t) \rangle = \gamma \mu'_y \mu'_z \tag{10}$$

That is, any rotationally-fixed, freely-rotating, or partially-rotating molecule's second-moment orientation vector $\boldsymbol{M}$ is equivalent to the linear superposition of a rotationally-fixed dipole of orientation $\boldsymbol{M}' = \left[\mu'_x, \mu'_y, \mu'_z, \mu'_x\mu'_y, \mu'_x\mu'_z, \mu'_y\mu'_z\right]^T$ of strength γ and an isotropic emitter of strength $(1-\gamma)$. The parameter γ can be physically interpreted as the rotational constraint of the molecule; $\gamma = 0$ corresponds to a completely rotationally mobile molecule.

We developed a maximum likelihood estimator to measure the brightness I_0, orientation (μ_x, μ_y), and rotational constraint γ of a molecule from a vector of measured spot brightnesses $\boldsymbol{I}_{\mathrm{spot}}$ of the Tri-spot PSF. The MATLAB function `fmincon` was used to maximize the log-likelihood function $\Lambda(I_0, \mu_x, \mu_y, \gamma)$ given by

$$\Lambda(I_0, \mu_x, \mu_y, \gamma) \propto \sum_{i=1}^{6} (\boldsymbol{s}_i + b_j) \ln(\boldsymbol{I}_{\mathrm{spot},i}(I_0, \mu_x, \mu_y, \gamma) + b_j) - (\boldsymbol{I}_{\mathrm{spot},i}(I_0, \mu_x, \mu_y, \gamma) + b_j) \tag{11}$$

where $\boldsymbol{s}_i = \left[s_{\mathrm{x1}}, s_{\mathrm{x2}}, s_{\mathrm{x3}}, s_{\mathrm{y1}}, s_{\mathrm{y2}}, s_{\mathrm{y3}}\right]^T$ is the measured spot brightnesses of the Tri-spot PSF across the x- and y-polarized channels of the microscope, b_j is the background measured in the x or y channel of the microscope, and $\boldsymbol{I}_{\mathrm{spot}}(I_0, \mu_x, \mu_y, \gamma)$ are the spot brightnesses predicted by our forward model using Equations (4)-(10).

We evaluated estimator performance by simulating 100 images at each point in orientation space (μ_x, μ_y, γ) of the Tri-spot PSF with 20,000 signal photons and 20 background photons/pixel. An example measurement is shown in Figure 3, where the noisy image input to the estimator agrees well with the recovered image generated from MLE.

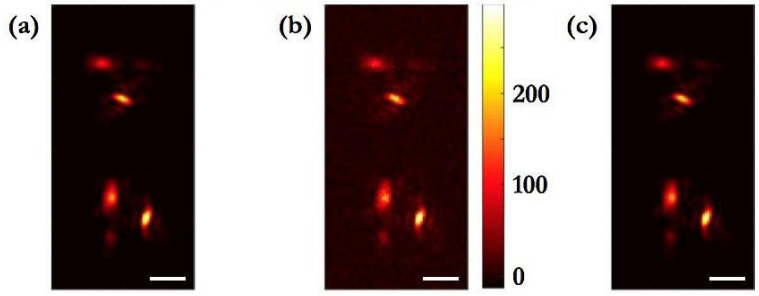

Figure 3. Orientation measurement using MLE. (a) Ground-truth image $I_{x(y)}$ without noise corresponding to orientation $(\mu_x = 0.48, \mu_y = 0.64)$ and rotational constraint $\gamma = 0.75$. (b) Simulated image with Poisson noise corresponding to 20,000 photons collected from the molecule and a background of 20 photons/pixel. Color bar in units of photons/pixel. (c) Recovered image of the molecule by MLE with orientation $(\mu_x = 0.486, \mu_y = 0.649)$ and rotational constraint $\gamma = 0.788$. Scale bar: 1 μm.

3.2 Characterizing measurement precision

The theoretical lower bound on the variance of any unbiased estimator is given by the Cramér-Rao lower bound (CRLB), which can be calculated using the inverse of the Fisher information matrix[23]. The appropriate choice of an estimator can yield measurement performance approaching the CRLB[24]. Here, we calculated the precision of our estimator as $\sigma_\theta = \mathrm{std}(\hat{\theta})$, where θ is the parameter to be estimated.

The spatial pattern of orientation measurement precision (Figure 4(a)) is similar to that of the best-possible measurement precision as calculated by $\sqrt{\mathrm{CRLB}}$ (Figure 4(b)). The orientation measurement precision of μ_x for most orientations is less than $1.5\sqrt{\mathrm{CRLB}}$, which indicates that MLE achieves good performance relative to the theoretical limits of the Tri-spot PSF. Overall, the precision of our MLE is 1.15 times larger than $\sqrt{\mathrm{CRLB}}$ for $\gamma = \{0.25, 0.5, 0.75\}$ and 1.08 times larger than $\sqrt{\mathrm{CRLB}}$ for $\gamma = 1$ when averaged across all possible molecular orientations.

3.3 Characterizing measurement accuracy

We evaluated the measurement bias of MLE by comparing the mean bias over 100 trials (Figure 5(a)) to the expected standard error given by

$$\mathrm{std}(\mathrm{bias}_\theta) = \frac{1}{\sqrt{100}}\sqrt{\mathrm{CRLB}_\theta} \tag{12}$$

Therefore, if MLE is sufficiently accurate, the ratio of bias_θ to $\sqrt{\mathrm{CRLB}_\theta}$ (Figure 5(b)) should be mostly confined to values $\pm 3/\sqrt{100} = 0.3$. There are a set of orientations for $\gamma = \{0.25, 1\}$ that have larger bias than the aforementioned threshold. Since this bias appears to be deterministic as a function of orientation (μ_x, μ_y) and rotational constraint γ, we can remove the bias by using the measured bias (Figure 5(a)) as a calibration map to restore accuracy of the estimator.

Since the range of rotational constraint is bounded to $\hat{\gamma} \in [0, 1]$, the distributions of measured $\hat{\gamma}$ are not Gaussian near the edges of the domain, and we define measurement bias as the median of the measurements over 100 trials. Our MLE is also slightly biased (Figure 6) when estimating rotational constraint γ for small values of γ. However, this bias similarly appears to be deterministic with respect to rotational constraint, and the measured bias can be used as a calibration map.

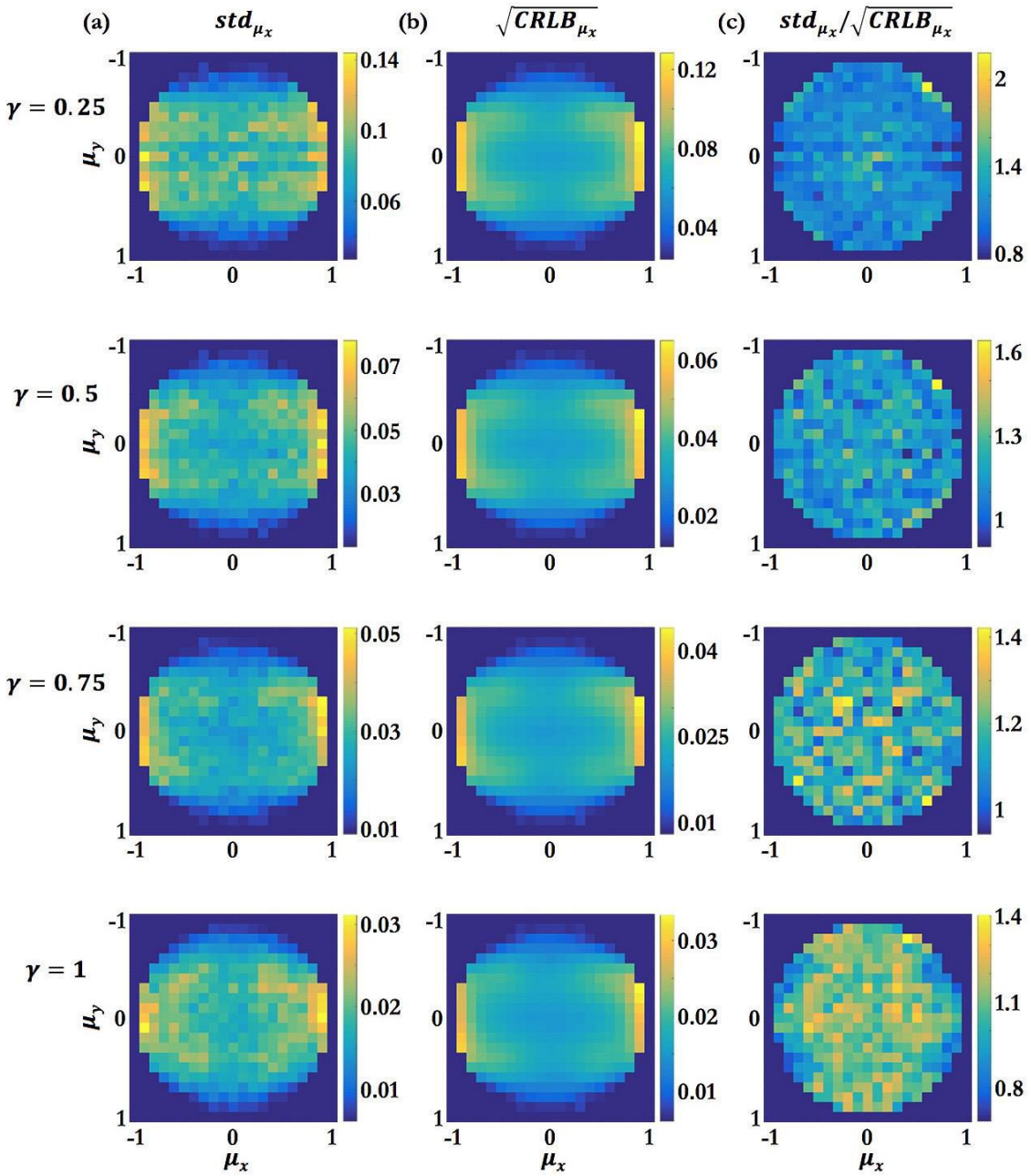

Figure 4. Precision of the Tri-spot PSF using MLE. (a) Precision of measuring orientation component μ_x for various orientations (μ_x, μ_y) and rotational constraints $\gamma = \{0.25, 0.5, 0.75, 1\}$. (b) Theoretical best-possible measurement precision of μ_x, as computed by $\sqrt{\text{CRLB}}$. (c) The ratio of the precision of MLE to the best-possible measurement precision.

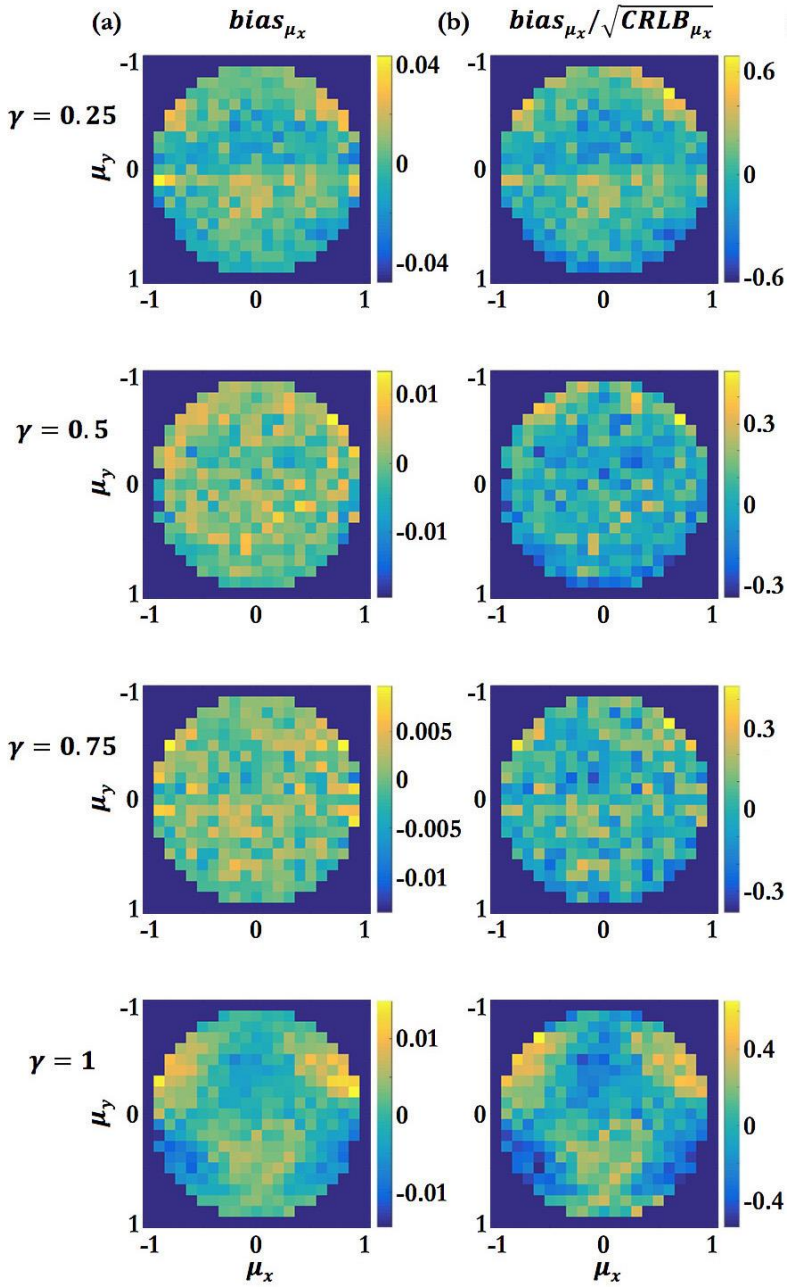

Figure 5. Accuracy of the Tri-spot PSF using MLE. (a) Average estimation bias of μ_x across 100 simulated trials for various orientations (μ_x, μ_y) and rotational constraints $\gamma = \{0.25, 0.5, 0.75, 1\}$. (b) Estimation bias compared to $\sqrt{\text{CRLB}}$. For 100 trials, these values should be mostly confined to within ± 0.3 for a sufficiently accurate estimator.

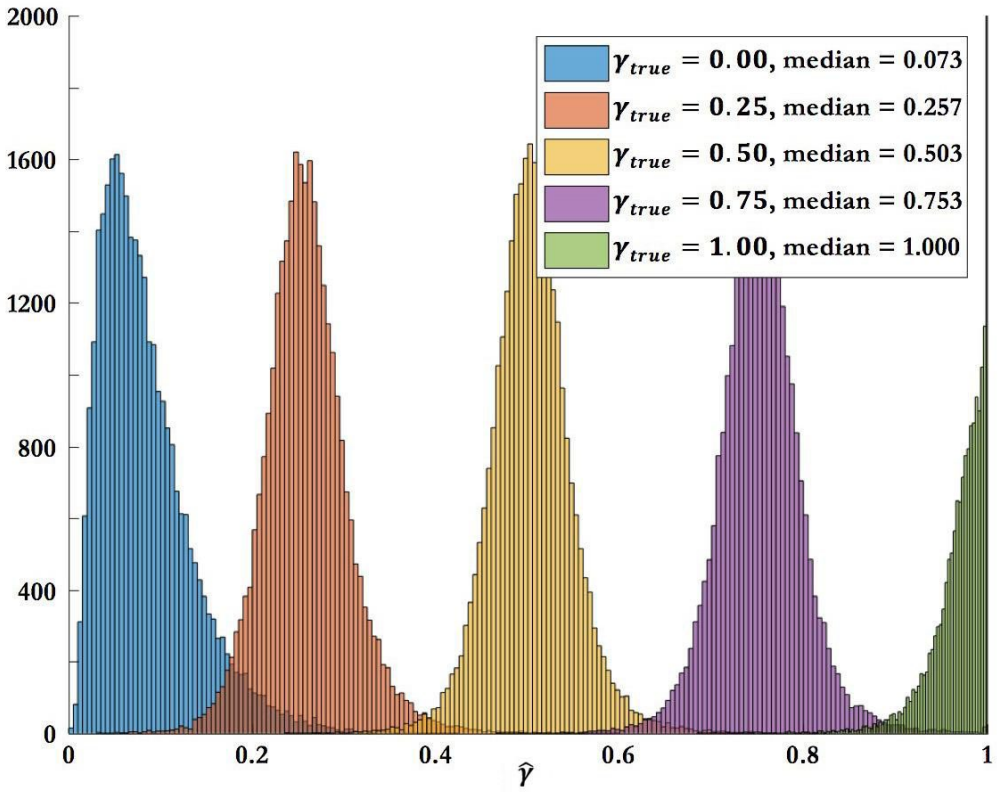

Figure 6. Accuracy of measuring rotational constraint γ for the Tri-spot PSF using MLE on 30,900 simulated images spanning all possible molecular orientations. For the ground-truth rotational constraints $\gamma = \{0,0.25,0.5,0.75,1\}$, the median estimates of rotational constraint are given by $\hat{\gamma} = \{0.073,0.257,0.503,0.753,1.000\}$, averaged over all possible orientations (μ_x, μ_y). In our implementation of MLE, the estimates of rotational constraint are bounded to the range $\hat{\gamma} \in [0,1]$.

4. MEASURING THE ORIENTATION OF SINGLE MOLECULES

4.1 Experimental setup

To create a sample containing rotationally-fixed dipole emitters, we embedded CF640R Amine (Biotium, 92043) in a thin film of 1% PMMA (poly methyl methacrylate, Aldrich Chemistry 182265) on top of a high-tolerance No. 1.5 glass coverslip. The sample was excited by a 637-nm laser (peak intensity 3.41 kW/cm^2). The fluorescence was collected using a custom-built epifluorescence microscope (1.4 NA Olympus objective lens, UPLSAPO100XO) with two orthogonally-polarized imaging channels[22], and the Tri-spot phase mask was loaded as the mask pattern on a liquid-crystal spatial light modulator (Meadowlark, 256 XY Phase Series) placed in the Fourier plane of the microscope. The images were captured using a scientific CMOS camera (Hamamatsu C11440-22CU) with 150 ms exposure time. An example image of a CF640R molecule is shown in Figure 7.

4.2 Orientation measurements using the Tri-spot PSF

Using MLE, we measured the orientation and rotational constraint of two molecules embedded in the polymer film (Figure 8). Due to crosslinking of the polymer matrix, we expect the rotational constraint of each molecule to be nearly unity. The median rotational constraint measured for 21 molecules is $\hat{\gamma} = 1$ as expected (Figure 9(a)). Comparing the experimentally-measured distribution to that of a simulated rotationally-fixed dipole emitter (Figure 9(b)) reveals that the two distributions are similar in shape. Measurements that significantly deviate from $\hat{\gamma} = 1$ could result from optical aberrations or variations in the local environment surrounding particular molecules.

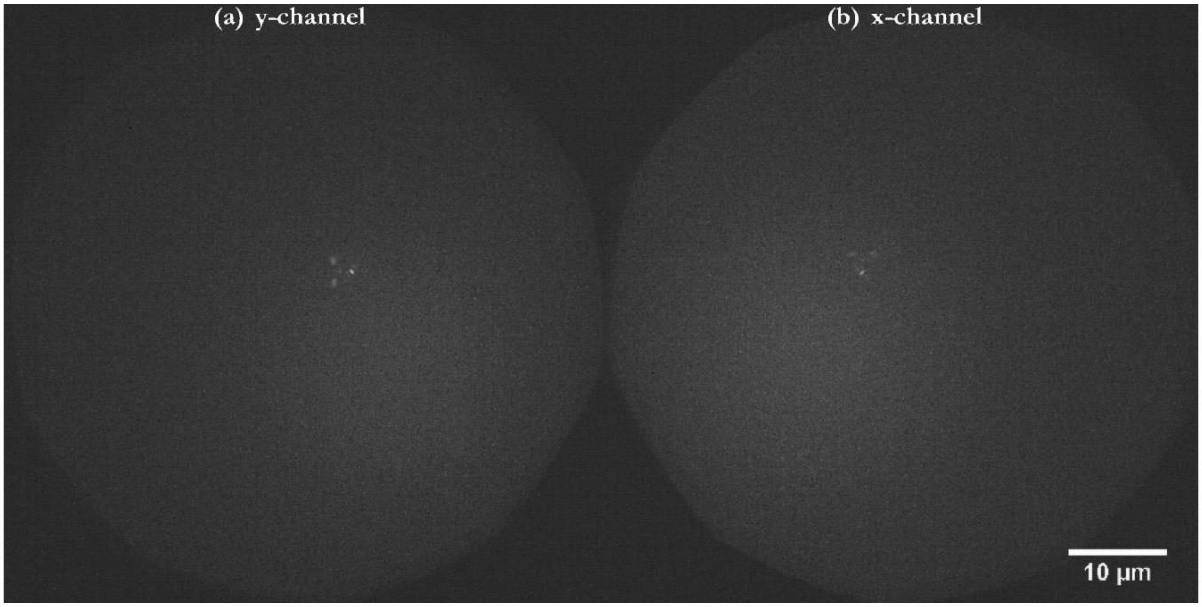

Figure 7. Raw image of one CF640R fluorescent molecule. (a) y-polarized imaging channel. (b) x-polarized imaging channel. The images contain a total of 11789 photons from the molecule with a local average background of 9.37 photons/pixel. Scale bar: 10 μm.

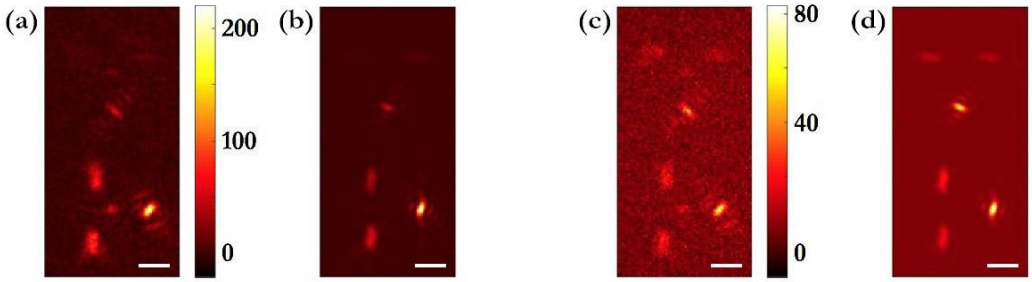

Figure 8. Orientation measurements of two single-molecule emitters. The maximum likelihood estimator used one image of each molecule to estimate its orientation. (a) Raw image of molecule 1 with 5195 photons detected. (b) Recovered image of molecule 1 using MLE with orientation $(\mu_x = -0.35, \mu_y = -0.92)$ and rotational constraint $\gamma = 1.00$. (c) Raw image of molecule 2 with 2492 photons detected. (d) Recovered image of molecule 2 using MLE with orientation $(\mu_x = 0.59, \mu_y = 0.81)$ and rotational constraint $\gamma = 0.86$. Color bar in units of photons/pixel. Scale bar: 1 μm.

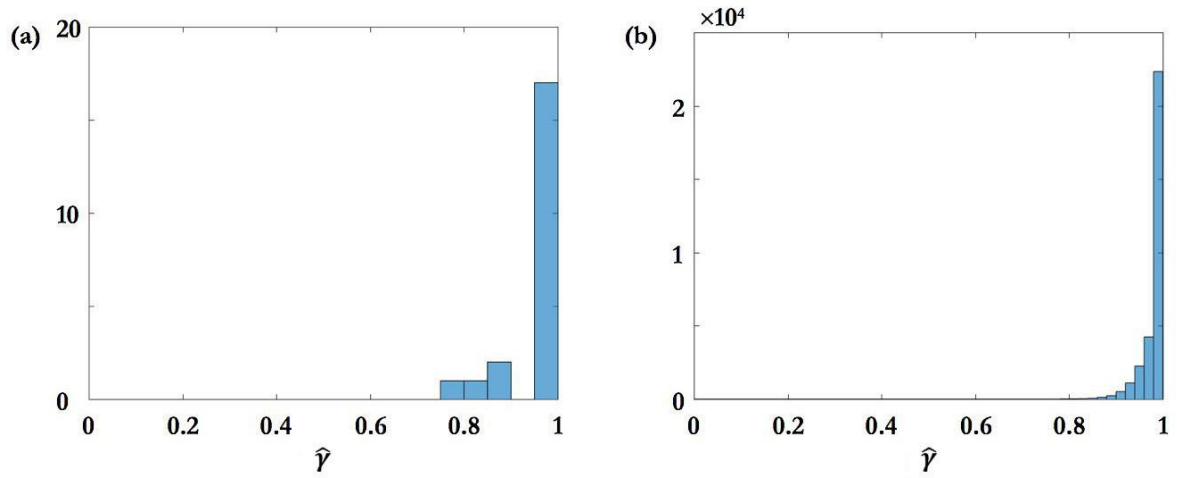

Figure 9. Measured rotational constraint of single-molecule emitters using the Tri-spot PSF. (a) Experimental distribution of estimated rotational constraints $\hat{\gamma}$ for 21 emitters embedded in a thin polymer film. (b) Simulated distribution of estimated rotational constraints $\hat{\gamma}$ for 30900 images of rotationally-fixed molecules with 20000 photons detected and 20 photons/pixel fluorescence background.

5. CONCLUSION

We developed a Tri-spot PSF that enables the measurement of the orientation and rotational mobility of single fluorescent molecules. We characterized the precision and accuracy of MLE using simulated images of the Tri-spot PSF. Measurements of molecular orientation and rotational mobility were accurate to within standard error, and the precision of MLE approached the theoretical limit given by $\sqrt{\text{CRLB}}$. We also demonstrated the Tri-spot PSF for measuring the orientation of molecules embedded in a thin polymer film, and measurements revealed that these molecules were fixed in orientation as expected.

In the future, the signal-to-background ratio of the Tri-spot PSF can be improved by optimizing the mask to minimize zero-order diffraction leakage, thereby improving measurement precision and accuracy. Further, a combined position and orientation estimator can be developed for generated localization and orientation images in single-molecule super-resolution microscopy.

6. ACKNOWLEDGEMENTS

Research reported in this publication was supported by the National Science Foundation under grant number ECCS-1653777 and by the National Institute of General Medical Sciences of the National Institutes of Health under grant number R35GM124858.

REFERENCES

[1] Moerner, W. E. and Kador, L., "Optical detection and spectroscopy of single molecules in a solid," Phys. Rev. Lett. **62**(21), 2535–2538 (1989).

[2] Betzig, E., "Single Molecules, Cells, and Super-Resolution Optics (Nobel Lecture)," Angew. Chemie Int. Ed. **54**(28), 8034–8053 (2015).

[3] Hell, S. W., "Nanoscopy with Focused Light (Nobel Lecture)," Angew. Chemie Int. Ed. **54**(28), 8054–8066 (2015).

[4] Moerner, W. E., "Single-Molecule Spectroscopy, Imaging, and Photocontrol: Foundations for Super-Resolution Microscopy (Nobel Lecture)," Angew. Chemie Int. Ed. **54**(28), 8067–8093 (2015).

[5] Backlund, M. P., Lew, M. D., Backer, A. S., Sahl, S. J. and Moerner, W. E., "The Role of Molecular Dipole Orientation in Single-Molecule Fluorescence Microscopy and Implications for Super-Resolution Imaging," ChemPhysChem **15**(4), 587–599 (2014).

[6] Corrie, J. E., Brandmeier, B. D., Ferguson, R. E., Trentham, D. R., Kendrick-Jones, J., Hopkins, S. C., van der Heide, U. A., Goldman, Y. E., Sabido-David, C., Dale, R. E., Criddle, S. and Irving, M., "Dynamic measurement of myosin light-chain-domain tilt and twist in muscle contraction.," Nature **400**(6743), 425–430 (1999).
[7] Peterman, E. J. G., Sosa, H., Goldstein, L. S. B. and Moerner, W. E., "Polarized Fluorescence Microscopy of Individual and Many Kinesin Motors Bound to Axonemal Microtubules," Biophys. J. **81**(5), 2851–2863 (2001).
[8] Sosa, H., Peterman, E. J. G., Moerner, W. E. and Goldstein, L. S. B., "ADP-induced rocking of the kinesin motor domain revealed by single-molecule fluorescence polarization microscopy," Nat. Struct. Biol. **8**(6), 540–544 (2001).
[9] Forkey, J. N., Quinlan, M. E. and Goldman, Y. E., "Protein structural dynamics by single-molecule fluorescence polarization.," Prog. Biophys. Mol. Biol. **74**(1–2), 1–35 (2000).
[10] Backer, A. S., Lee, M. Y. and Moerner, W. E., "Enhanced DNA imaging using super-resolution microscopy and simultaneous single-molecule orientation measurements," Optica **3**(6), 659 (2016).
[11] Rosenberg, S. a, Quinlan, M. E., Forkey, J. N. and Goldman, Y. E., "Rotational motions of macro-molecules by single-molecule fluorescence microscopy.," Acc. Chem. Res. **38**(7), 583–593 (2005).
[12] Lieb, M. A., Zavislan, J. M. and Novotny, L., "Single-molecule orientations determined by direct emission pattern imaging," J. Opt. Soc. Am. B **21**(6), 1210 (2004).
[13] Backer, A. S. and Moerner, W. E., "Extending single-molecule microscopy using optical fourier processing.," J. Phys. Chem. B **118**(28), 8313–8329 (2014).
[14] Pavani, S. R. P., Thompson, M. A., Biteen, J. S., Lord, S. J., Liu, N., Twieg, R. J., Piestun, R. and Moerner, W. E., "Three-dimensional, single-molecule fluorescence imaging beyond the diffraction limit by using a double-helix point spread function," Proc. Natl. Acad. Sci. **106**(9), 2995–2999 (2009).
[15] Lew, M. D., Lee, S. F., Badieirostami, M. and Moerner, W. E., "Corkscrew point spread function for far-field three-dimensional nanoscale localization of pointlike objects.," Opt. Lett. **36**(2), 202–204 (2011).
[16] Jia, S., Vaughan, J. C. and Zhuang, X., "Isotropic three-dimensional super-resolution imaging with a self-bending point spread function," Nat. Photonics **8**(4), 302–306 (2014).
[17] Shechtman, Y., Weiss, L. E., Backer, A. S., Sahl, S. J. and Moerner, W. E., "Precise Three-Dimensional Scan-Free Multiple-Particle Tracking over Large Axial Ranges with Tetrapod Point Spread Functions," Nano Lett. **15**(6), 4194–4199 (2015).
[18] von Diezmann, A., Shechtman, Y. and Moerner, W. E., "Three-Dimensional Localization of Single Molecules for Super-Resolution Imaging and Single-Particle Tracking," Chem. Rev. **117**(11), 7244–7275 (2017).
[19] Shechtman, Y., Weiss, L. E., Backer, A. S., Lee, M. Y. and Moerner, W. E., "Multicolour localization microscopy by point-spread-function engineering," Nat. Photonics **10**(9), 590–594 (2016).
[20] Backer, A. S., Backlund, M. P., von Diezmann, A. R., Sahl, S. J. and Moerner, W. E., "A bisected pupil for studying single-molecule orientational dynamics and its application to three-dimensional super-resolution microscopy," Appl. Phys. Lett. **104**(19), 193701 (2014).
[21] Backer, A. S., Backlund, M. P., Lew, M. D. and Moerner, W. E., "Single-molecule orientation measurements with a quadrated pupil," Opt. Lett. **38**(9), 1521 (2013).
[22] Backlund, M. P., Lew, M. D., Backer, A. S., Sahl, S. J., Grover, G., Agrawal, A., Piestun, R. and Moerner, W. E., "Simultaneous, accurate measurement of the 3D position and orientation of single molecules.," Proc. Natl. Acad. Sci. U. S. A. **109**(47), 19087–19092 (2012).
[23] Kay, S. M., [Fundamentals of statistical signal processing], Prentice Hall, Englewood Cliffs, N.J. (1993).
[24] Shechtman, Y., Sahl, S. J., Backer, A. S. and Moerner, W. E., "Optimal Point Spread Function Design for 3D Imaging," Phys. Rev. Lett. **113**(13), 133902 (2014).